Research Square

Preprints are preliminary reports that have not undergone peer review.
They should not be considered conclusive, used to inform clinical practice,
or referenced by the media as validated information.

FTIR-Derived Vibrational Hardening and Elastic Metrics in Bi-Doped Co-Zn Spinel Ferrite Nanoparticles

Italo Nuta
Universidade Federal de Goiás
Thiago Eduardo Pereira Alves
Universidade Federal de Goiás
Prasun Banerjee
Gandhi Institute of Technology and Management (GITAM) University
A. Franco
franco@ufg.br

Universidade Federal de Goiás

Research Article

Keywords:

Posted Date: April 13th, 2026

DOI: https://doi.org/10.21203/rs.3.rs-9270866/v1

License: This work is licensed under a Creative Commons Attribution 4.0 International License.
Read Full License

Additional Declarations: No competing interests reported.

FTIR-Derived Vibrational Hardening and Elastic Metrics in Bi-Doped Co-Zn Spinel Ferrite Nanoparticles

Italo Nuta
Instituto de Física
Universidade Federal de Goiás, Goiânia, Brazil

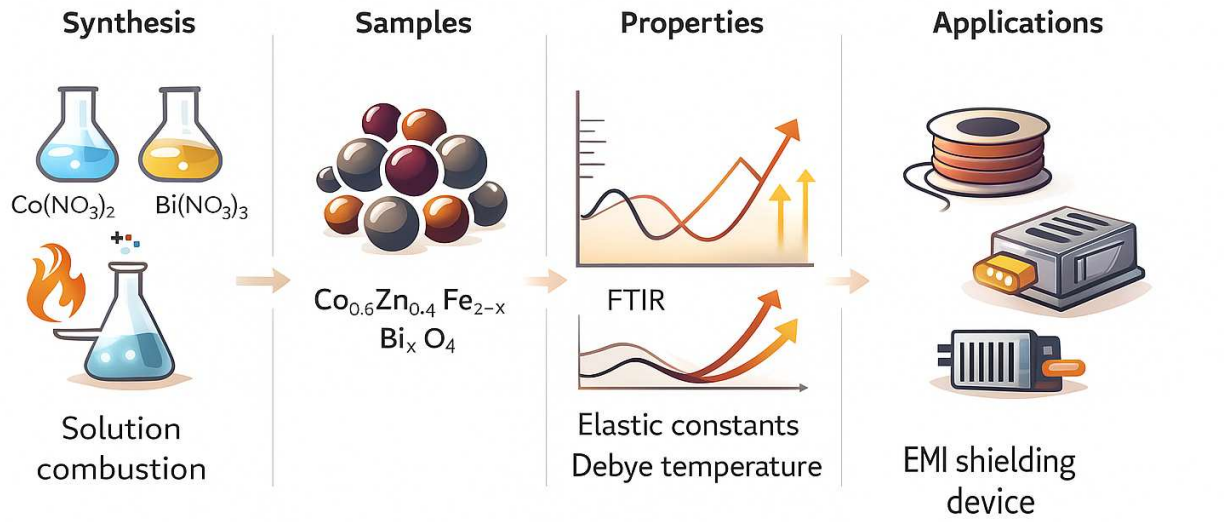
Thiago Eduardo Pereira Alves
Instituto Federal de Goiás, Goiânia, Brazil

Prasun Banerjee
Multidisciplinary Unit of Research on Translational Initiatives (MURTI) MMMRL Lab
Gandhi Institute of Technology and Management (GITAM) University
Bengaluru, Karnataka, India

A. Franco Jr.
Instituto de Física
Universidade Federal de Goiás, Goiânia, Brazil
e-mail: {franco}@ufg.br

Abstract

Spinel ferrites are technologically important materials whose properties can be tuned by doping. In this study, we examine how nominal Bi addition ($0 \leq x \leq 0.03$) in Co-Zn ferrite nanoparticles modifies metal-oxygen vibrational features and derived elastic metrics of FTIR spectroscopy. $Co_{0.6}Zn_{0.4}Fe_{2-x}Bi_xO_4$ nanoparticles were synthesized via solution combustion, and FTIR spectra were used to probe the tetrahedral (ν_A) and octahedral (ν_B) metal-oxygen vibrational contributions. FTIR peak fitting indicates a reproducible blue-shift of the octahedral contribution while ν_A remains same. Effective elastic constants (C_{11}, C_{12}) and moduli (E, G, B) estimated from IR-derived force constants show an increasing trend with *Bi* content, and the Debye parameters derived from optical wave-numbers (θ_D^I) and acoustic velocities (θ_D^E) increase comparably within propagated uncertainties. Overall, the observed trends suggest vibrational hardening and increased effective stiffness with *Bi* addition.



Graphical Abstract

1 Introduction

Spinel ferrite materials are technologically important due to their versatile magnetic and mechanical properties, finding applications in devices such as transformers, inductors, and magnetic sensors [1]. Infrared (IR) spectroscopy is widely recognized as a powerful analytical tool for chemical identification and structural characterization. Its main advantage over other structural techniques lies in its ability to provide rapid and reliable information about molecular structure using only a small amount of material, without requiring complex analytical procedures. The technique is based on the selective absorption of infrared radiation by a material, which depends on the vibrational frequencies of its molecular bonds. The resulting absorption bands correspond to characteristic functional groups and bonding environments within the compound [2, 3]. In spinel ferrite systems, these absorption features can be distinguished according to the vibrations of cations occupying tetrahedral (A) and octahedral (B) sites in the crystal lattice . As reported by Waldron [4], the infrared spectra of spinel ferrites generally exhibit two principal absorption bands: a high-frequency band (580-605 cm^{-1}) associated with A-site vibrations and a low-frequency band (408-425 cm^{-1}) corresponding to B-site vibrations. These two characteristic bands arise from the difference in $Fe^{3+} - O^{2-}$ bond lengths between the A and B sites. Such M-O vibrational band assignments have been consistently observed across various cobalt and mixed spinel ferrites [5].

The investigation of the elastic properties of ferrite materials is fundamentally important for understanding the intrinsic bonding mechanisms at the atomic scale. Such elastic constants directly determine the Debye temperature, linking

mechanical stiffness to lattice thermal properties [6]. These studies provide valuable insights into interatomic and interionic forces, lattice stability, and the coupling between mechanical and thermal behaviors of solids [7]. Indeed, gradual compositional changes in ferrites have been observed to systematically shift the Debye temperature by modifying vibrational frequencies and bond strengths [8]. Notably, the Debye temperature can be derived from the elastic properties of a material, as it is directly proportional to the average sound velocity, which in turn depends on the elastic constants. This approach allows for the estimation of the Debye temperature without the need for specific-heat measurements, particularly advantageous at very low temperatures, where the relationship between vibrational and elastic properties is most pronounced.

Moreover, in ferrites, mechanical stress can induce variations in magnetization through magnetostrictive and piezomagnetic effects, while sudden mechanical shocks may trigger domain-wall motion and energy dissipation. Conversely, changes in magnetic order can also influence lattice dynamics in magnetostrictive materials. An intriguing characteristic of cobalt ferrites substituted with nonmagnetic Zn^{2+} ions is the enhancement of their saturation magnetization. This effect occurs because Zn^{2+} ions preferentially occupy the tetrahedral (A) sites, similar to their behavior in pure zinc ferrite, thereby reducing the A-site contribution to the overall magnetization. Consequently, partial Zn substitution (e.g., 10 mol% in $Co_{0.9}Zn_{0.1}Fe_2O_4$) leads to an increase in the magnetization of $CoFe_2O_4$ by approximately $0.8\mu_B$ per formula unit. Similarly, substitution with heavy trivalent ions like Bi^{3+} is known to alter cation distributions and anisotropy in spinel ferrites. Thus, we anticipate that introducing Bi^{3+} into Co-Zn ferrite could significantly affect its lattice vibrational properties.

This work addresses that gap by examining how low-level Bi addition ($x \leq 0.03$) influences the vibrational spectrum and IR-derived elastic parameters of Co–Zn ferrite nanoparticles via FTIR analysis. The novelty of this work lies in reporting reproducible FTIR peak shifts with uncertainty quantification and mapping these spectral trends onto effective elastic metrics using established semi-empirical IR–elasticity relations. Importantly, this study is intentionally limited to FTIR-accessible vibrational signatures and derived elastic metrics. It does not claim crystallographic proof of Bi site occupancy or verified elemental stoichiometry without independent structural probes.

2 Experimental procedure

A series of $Co_{0.6}Zn_{0.4}Fe_{2-x}Bi_xO_4$ ($0 \leq x \leq 0.03$) nanoparticles with nominal compositions of x= 0.0, 0.005, 0.01, and 0.03 mol were synthesized using the combustion reaction method [9]. The compositions are nominal and are defined by precursor stoichiometry; no independent elemental quantification was performed in this work. The Bi^{3+} doping range was limited to x = 0.03 to avoid the formation of secondary phases, as higher Bi content can exceed the solubility in the spinel lattice and induce impurity phases. This low solubility is expected due to the large ionic radius mismatch between Bi^{3+} and the host spinel cations. However, in the absence of diffraction refinement, this work does not report lattice-parameter trends as evidence of substitution and instead focuses on spectroscopic trends. Analytical-grade reagents from Aldrich (New Jersey, USA) were used, including cobalt nitrate ($Co(NO_3)_2 \cdot 6H_2O$), bismuth nitrate ($Bi(NO_3)_3 \cdot 5H_2O$), iron nitrate ($Fe(NO_3)_3 \cdot 9H_2O$), and urea ($CO(NH_2)_2$) as fuel. Urea was selected as the fuel because its high nitrogen content

and exothermic decomposition facilitate a self-sustaining combustion reaction, yielding homogeneous and fine ferrite powders. For each composition, appropriate amounts of nitrates and fuel were dissolved in deionized water (Milli-Q) in a wide-mouth glass basin. The mixture was stirred until a homogeneous solution formed, then placed on a preheated hot plate (approximately 400°C) in a ventilated fume hood. Within minutes, the solution began to boil, releasing water vapor, followed by the emission of additional gases. This process culminated in ignition, producing an intense flame (approximately 1000°C), which rapidly converted the solution into a fragile foam that disintegrated into a fine powder with slight agitation. No additional calcination or sintering was performed. Therefore, the present study reports FTIR-accessible vibrational signatures of the as-prepared powders and derived elastic trends without using XRD-based phase identification or crystallographic refinement.

Infrared spectra (FT-IR) were obtained using a Perkin-Elmer Spectrum System 400, with samples prepared in KBr pellets (1%) and measured across the 380-4000 cm^{-1} range. All FTIR measurements were performed in triplicate using independently prepared KBr pellets to ensure reproducibility. Peak positions were extracted using Lorentzian fitting, and uncertainties were determined from standard deviation across measurements. The instrumental resolution of the FTIR spectrometer was 2 cm^{-1}, and reported peak shifts exceeding this resolution were considered statistically significant.

3 Result and discussions

3.1 FTIR Spectral Features and Phase Integrity

The FTIR spectra of pure cobalt–zinc ferrite ($CoFe_2O_4$) and Bi-doped Co-Zn ferrite nanoparticles ($Co_{0.6}Zn_{0.4}Fe_{2-x}Bi_xO_4$, for x = 0, 0.005, 0.010, and 0.030) are shown in Fig. 1, revealing the two characteristic spinel ferrite absorption bands centered at $571 \pm 2\,\mathrm{cm}^{-1}$ and $386 \pm 2\,\mathrm{cm}^{-1}$. These two contributions correspond to metal-oxygen stretching vibrations associated with tetrahedral (A) and octahedral (B) coordination environments in spinel ferrites and are assigned as ν_A and ν_B, respectively. Within the mid-IR sensitivity of FTIR, no obvious additional absorption bands are observed upon Bi addition; however, FTIR alone cannot exclude trace or nano-crystalline secondary phases at grain boundaries, and phase purity cannot be claimed without diffraction analysis.

With increasing Bi content, both ν_A and ν_B bands shift to higher wavenumbers (blue-shift), indicating a discernible change in lattice vibrational dynamics. This indicates that the effective local bond stiffness associated with the octahedral vibrational contribution increases with Bi addition, but this spectroscopic trend does not by itself prove crystallographic bond contraction. In particular, the octahedral-site band ν_B moves from 387±2 cm^{-1} for x = 0 to 392±2 cm^{-1} for x = 0.03, whereas the tetrahedral band ν_A remains approximately constant around 568±2 cm^{-1} (Table 1). This blue-shift suggests an increase in the effective force constant of the vibrational mode contributing to ν_B. Because vibrational frequencies in complex spinels reflect coupled lattice dynamics, the shift is interpreted as vibrational hardening rather than direct proof of bond-length contraction.

These results reveal that even a small Bi addition measurably stiffens the lattice vibration modes, which could influence the material's elastic and magnetic properties. Similar FTIR features (two main peaks near 400 and 593 cm^{-1}) were

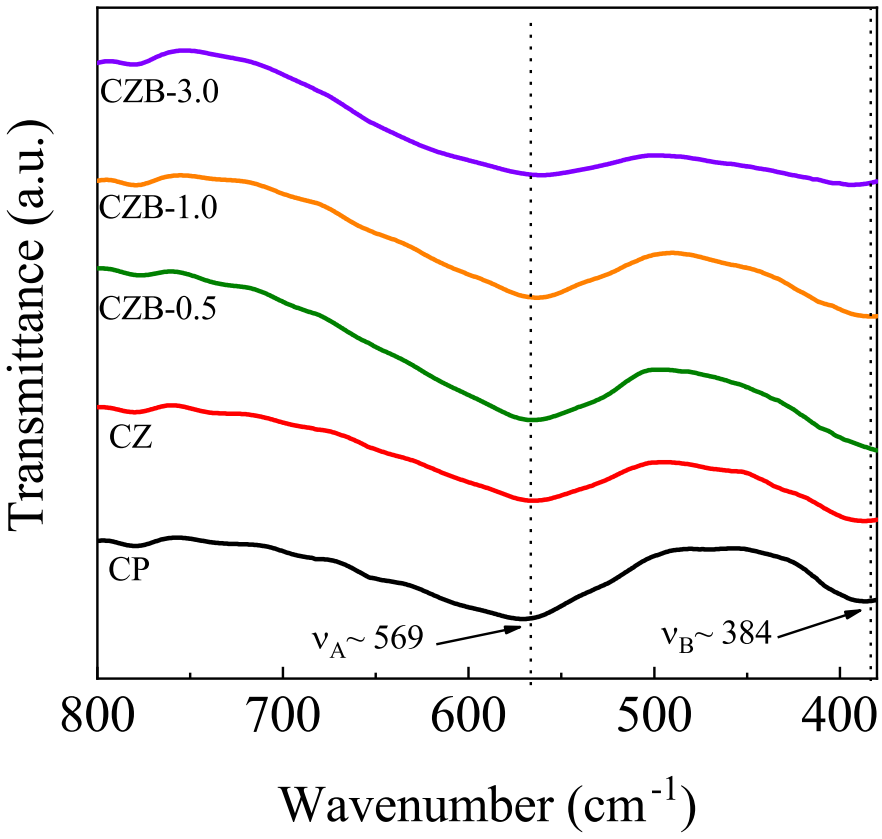


Figure 1 Room temperature FTIR spectra for $CoFe_2O_4$ and $Co_{0.6}Zn_{0.4}Fe_{2-x}Bi_xO_4$ (with $x = 0.00, 0.005, 0.010, 0.03$ mol) samples, showing fitted ν_A and ν_B peak positions ($\pm 2cm^{-1}$) extracted from triplicate pellets.

reported by Batoo et al. [10] in Bi-doped Co–Zn ferrites, supporting our band assignments. This highlights FTIR as a rapid tool to assess doping-induced bond changes in spinel ferrites. Future studies might include temperature-dependent vibrational spectroscopy or complementary techniques (e.g., Raman) to further explore these bond-stiffening effects.

3.2 Cation Distribution and Vibrational Dynamics

The vibrational frequency behavior can be explained by the inverse relation between the vibrational frequency (ν) and the reduced mass (μ) of the bond, as given by

$$\nu = \frac{1}{2\pi c}\sqrt{\frac{k}{\mu}}, \tag{1}$$

where m_1 and m_2 are the atomic masses of the two bonded atoms, c is the speed of light, and k is the bond force constant.

In the present case, substitution of the much heavier Bi^{3+} ion (molar mass 208.98 g/mol) in place of Fe^{3+} (55.85 g/mol) is expected to influence ν_A and ν_B by increasing the reduced mass μ. On its own, a larger μ would tend to drive the vibrational frequency lower; however, Bi^{3+} substitution simultaneously perturbs the lattice and can alter the effective spring constant k of the bonds (Eq. 1). Bi^{3+} is often expected to favor octahedral coordination in spinel-type environments

Table 1 FTIR parameters at room temperature for $CoFe_2O_4$ and $Co_{0.6}Zn_{0.4}Fe_{2-x}Bi_xO_4$ (with $x = 0.00, 0.005, 0.010, 0.03$ mol) samples.

Samples	x(mol)	M_A (g/mol)	M_B $g/mol)$	ν_A (cm^{-1})	ν_B (cm^{-1})	ν_{av} (cm^{-1})	K_A (N/m)	K_B (N/m)	K_{av} (N/m)
$CoFe_2O_4$		55.84	114.78	569±2	384±2	476±1.4	138.7±1.0	90.8±0.9	114.8±0.7
$Co_{0.6}Zn_{0.4}Fe_{2-x}Bi_xO_4$	0.000	55.84	117.37	568±2	387±2	477±1.4	135.8±1.0	93.3±0.9	114.6±0.7
	0.005	56.61	117.37	569±2	387 ± 2	478±1.4	137.7±1.0	90.0±0.9	113.8±0.7
	0.010	57.38	117.37	568±2	391 ± 2	479±1.4	138.6±1.0	91.4±0.9	115.9±0.7
	0.030	60.44	117.37	568±2	392±2	481±1.4	144.4±1.0	90.9±0.9	117.7±0.7

based on crystal-chemical arguments. Specific cation redistribution pathways (e.g., Co^{2+} migration between A/B sites) cannot be uniq established from FTIR peak shifts alone. If cation redistribution occurs, it could influence local force constants and coupled vibrational mode.

Such changes in cation positions and ionic sizes will modify the equilibrium metal-oxygen bond lengths in the lattice. In principle, introducing a larger cation can increase average bond lengths and thus red-shift vibrational modes. However, the experimentally observed blue-shift indicates that an increase in the effective restoring force (force constant) outweighs reduced-mass and average-size effects for the vibrational contribution dominating ν_B (Fig. 1 and Table 1). This indicates vibrational hardening (higher effective force constants) of the relevant coupled mode. In other words, the IR-derived elastic metrics increase with x within uncertainty, and this trend correlates with an increase in the Debye parameters reported here. According to the Debye model, a solid is treated as an elastic continuum, in which the Debye temperature (θ_D) is defined by the maximum frequency of lattice vibrations and is directly related to the sound velocity within the material.

Thus, the Debye temperature (θ_D^I) for all samples was calculated using the average frequency of the FTIR absorption bands, as expressed by the following relation:[11]:

$$\theta_D^I = \frac{hc}{k_B}\nu_{av} \tag{2}$$

where h ($= 6.626 \times 10^{-34}$ J s) is Planck's constant, k_B ($= 1.380 \times 10^{-23}$ J/K) is Boltzmann's constant, c ($= 3 \times 10^8$ m/s) is the speed of light, ν_{av} represents the average frequency of the IR bands. These frequency bands are related to force constant at A-sites and B- sites respectively. The identified frequency bands are associated with the stretching vibrations of metal-oxygen bonds at the A-and B-sites, reflecting their respective force constants. As illustrated in Figure 2 and Table 4, the Debye temperature exhibits a slight but consistent increase with increasing Bi content. Future work could involve direct probes (e.g., Mössbauer or X-ray absorption spectroscopy) to confirm the cation site occupancy, as well as inelastic scattering experiments to map phonon changes with doping.

Table 2 Input parameters at room temperature for $CoFe_2O_4$ and $Co_{0.6}Zn_{0.4}Fe_{2-x}Bi_xO_4$ samples ($x = 0.00,\ 0.005,\ 0.010,$ and $0.030mol$) and the stiffness constants.

Samples	x(mol)	a (Å)	ρ_{Th} (g/cm^3)	ρ_{app} (g/cm^3)	p ($\times 10^{-2}$)	σ	C_{11} (GPa)	C_{12} (GPa)
$CoFe_2O_4$		8.37 ± 0.02	5.31±0.02	5.31±0.02	0±0.53	0.324±0.002	137.1±0.9	65.7±0.7
$Co_{0.6}Zn_{0.4}Fe_{2-x}Bi_xO_4$	0.000	8.37±0.02	5.37±0.02	5.27±0.02	1.84±0.52	0.318±0.002	135.9±0.9	63.8±0.7
	0.005	8.39±0.02	5.39±0.02	5.26±0.02	2.34±0.52	0.316±0.002	135.6±0.9	62.7±0.6
	0.010	8.40±0.02	5.41±0.02	5.26±0.02	2.69±0.52	0.315±0.002	136.9±0.9	62.9±0.6
	0.030	8.39±0.02	5.47±0.02	5.26±0.02	3.91±0.51	0.311±0.002	140.1±0.9	63.2±0.6

3.3 Elastic Constants and Mechanical Stiffness

The force constant (K) for tetrahedral site (K_A) and octahedral site (K_B) in N/m units can be calculated using relationships[4]:

$$K_A = 7.62x10^{-6}(M_A \nu_A^2) \tag{3}$$

$$K_B = 5.31x10^{-6}(M_B \nu_B^2) \tag{4}$$

where M_A and M_B are the molecular weight of A- and B -site respectively. ν_A e ν_B are the corresponding center frequency of tetrahedral site and octahedral site, respectively. The average bond stiffness was taken as the mean of these values:

$$K_{av} = \frac{K_A + K_B}{2} \tag{5}$$

From Table 1 it is evident that the tetrahedral bond force constant K_A increases with increasing Bi content, whereas the octahedral bond force constant K_B slightly decreases as x increases. This contrasting behavior is attributed to cation size and site-occupancy effects [4].

Elastic moduli provide valuable insights into a material's mechanical strength, fracture toughness, and resistance to thermal shock, critical properties for ensuring the successful integration of the material into functional devices. Elastic stiffness constants and moduli are key to understanding the interatomic bonding strength and mechanical stability of ferrites. The most commonly used parameters are Young's modulus (E), the shear (rigidity) modulus (G), and Poisson's ratio (σ). Young's modulus is particularly important in ferrites because it dictates the mechanical behavior of core components (such as rods and rings) under stress. In practice, when a ferrite is subjected to external influences (e.g., mechanical pressure, or temperature changes), internal stresses can develop, and the elastic moduli determine the material's ability to withstand deformation, fracture, or thermal shock during device operation.

In a cubic spinel (which exhibits nearly isotropic elastic behavior), there are only three independent elastic stiffness

Table 3 Elastic properties for $CoFe_2O_4$ and $Co_{0.6}Zn_{0.4}Fe_{2-x}Bi_xO_4$ (with $x = 0.00, 0.005, 0.010, 0.03$ mol) nanoparticles.

Samples	x (mol)	G (GPa)	B (GPa)	E (GPa)	V_l (m/s)	V_s (m/s)	V_m (m/s)
$CoFe_2O_4$		35.7±0.3	89.5±0.7	94.5±0.7	5081±16	2592±16	2905±17
$Co_{0.6}Zn_{0.4}Fe_{2-x}Bi_xO_4$	0.000	36.6±0.3	88.1±0.7	96.3±0.7	5096±16	2634±16	2948±17
	0.005	36.5±0.3	86.9±0.7	95.9±0.7	5076±16	2632±16	2950±17
	0.010	37.0±0.3	87.6±0.7	97.2±0.7	5102±16	2652±16	2968±17
	0.030	38.5±0.3	88.8±0.7	100.8±0.7	5161±16	2704±16	3025±17

coefficients [12]. We determined effective elastic moduli using IR-derived force constants together with input parameters (lattice parameter a, theoretical density ρ_{th}, and and apparent density ρ_{app} for porosity p estimation) as listed in Table 2.

The principal elastic stiffness constants C_{11} and C_{12} were calculated using the following relations [13, 14]:

$$C_{11} = \frac{K_{av}}{a} \tag{6}$$

$$C_{12} = \frac{\sigma C_{11}}{(1-\sigma)} \tag{7}$$

where σ is Poisson ratio and a is the lattice constant. Poisson's ratio, σ is a function of the pore fraction and is given by:

$$\sigma = 0.324(1 - 1.043p) \tag{8}$$

where f represents the sample's fraction porosity, defined as:

$$p = 1 - \left(\frac{\rho_{app}}{\rho}\right) \tag{9}$$

Here, ρ_{app} is the apprent density, and ρ is the theoretical density obtained from XRD data. The calculated Poisson's ratio ranges between 0.324 and 0.311. These values lie within the theoretical range of 0.5 to 0, confirming consistency with the theory of isotropic elasticity.

The variation in stiffness constants (C_{11} and C_{12}) as a function of Bi^{3+} content is displayed in Table 2. It can be seen that both stiffness constants increase with increasing Bi^{3+} content. The values of these stiffness constants are influenced by two factors: (*i*) the tightness of bonding between atoms and the force constant. In this system, the observed increase is reported as an effective stiffness trend produced by IR-derived force constants. These two stiffness constants are then used to calculate various elastic constants, such as Young's modulus (E), bulk modulus (B), and modulus of rigidity (G) as follows:

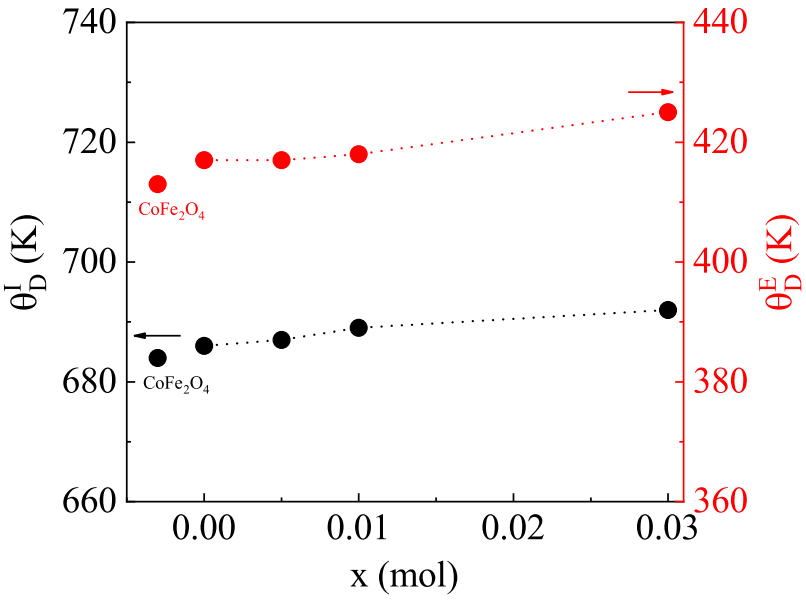


Figure 2 Comparison of Debye parameters derived from optical wavenumbers (θ_D^I) and elastic-wave analysis (θ_D^E) for $CoFe_2O_4$ and $Co_{0.6}Zn_{0.4}Fe_{2-x}Bi_xO_4$ (x = 0.00, 0.005, 0.010, and 0.030 mol).

$$B = \frac{1}{3}(C_{11} + 2C_{12}) \tag{10}$$

$$G = \frac{(2\sigma - 1)}{2(\sigma - 1)} C_{11} \tag{11}$$

$$E = \frac{(C_{11} - C_{12})(C_{11} + 2C_{12})}{(C_{11} + C_{12})} \tag{12}$$

The resulting values of E, B, and G for all compositions are given in Table 3. All three moduli show an overall increasing trend with higher Bi content (for example, E rises from 96.3±0.7 GPa at x = 0 to 100.8±0.7 GPa at x = 0.03). This improvement is reported as an effective stiffness trend derived from IR-based semi-empirical relations. As x increases, the IR-derived force constants and effective elastic metrics increase within uncertainty, consistent with vibrational hardening. Additionally, Bi-containing local environments may modify covalency and thus mode stiffness. Thus, the upward trend of *E*, *B*, and *G* with increasing Bi content demonstrates an increase in effective IR-derived stiffness metrics. These stiffer mechanical properties suggest that Bi doping can be used to tailor ferrite materials for applications requiring high rigidity. Future experiments (e.g., nanoindentation or resonant ultrasound) could directly measure these elastic constants to validate the IR-derived values.

3.4 Debye Temperature as a Lattice Rigidity Indicator

The Debye temperature is a useful gauge of bonding strength in a solid, as it represents the cutoff vibrational temperature (or highest normal mode frequency) of the lattice. From the elastic constants and densities, we calculated the sound velocities in the material. The longitudinal (V_l) and transverse (V_s) acoustic wave speeds were obtained via

$$V_l = \left(\frac{C_{11}}{\rho_{app}}\right)^{1/2} \tag{13}$$

$$V_S = \left(\frac{G_o}{\rho_{app}}\right)^{1/2} \tag{14}$$

where G_o is the modulus of rigidity corrected for zero pore fraction. These velocities were then used to determine the mean wave velocity (V_m) [13].

$$V_m = \left[\frac{1}{3}\left(\frac{1}{V_l^3} + \frac{2}{V_s^3}\right)\right]^{-1/3} \tag{15}$$

The variation of V_l, V_S, and V_m with Bi^{3+} content is illustrated in Fig. 3 and Table 2. The mean wave velocity was further used to calculate the Debye temperature (θ_D^E):

$$\theta_D^E = \frac{h}{k_B}\left(\frac{3q\rho_{app}N_A}{4\pi M_M}\right)^{1/3} V_m \tag{16}$$

where h is Planck's constant, k_B is Boltzmann's constant, and q is the number of atoms in the unit formula. N_A is the Avogadro's number, M_M is the molecular weight, and ρ_{app} is apparent density. Figure 2 compares compares the Debye parameters obtained from (i) optical/IR wavenumbers (θ_D^I) and (ii) acoustic-wave analysis (θ_D^E) for all samples.

Both the IR-derived Debye temperature θ_D^I (calculated from the average FTIR vibrational frequency, Eq. 2) and the elastic Debye temperature θ_D^E (from V_m, Eq. 16) show a steady rise as the Bi content increases. This indicates that incorporating Bi into the lattice raises the characteristic phonon energy scale of the ferrite, consistent with a stiffer lattice. However, the two Debye parameters differ substantially in magnitude because they probe different parts of the phonon spectrum and rely on different modeling assumptions.

In our samples, θ_D^I is larger than θ_D^E , which is expected because θ_D^I is anchored to high- frequency optical-mode wavenumbers whereas θ_D^E is determined by long-wavelength acoustic velocities and is also sensitive to porosity and nanoscale effects. This discrepancy can be attributed to their different physical origins (optical vs acoustic phonons), and in nanoparticles additional surface and grain-boundary scattering can decouple optical and acoustic responses relative to bulk assumptions. The parameter θ_D^I is influenced predominantly by short-range, high-frequency optical vibrational contributions localized to metal–oxygen bonding, whereas θ_D^E reflects long-wavelength acoustic stiffness within a continuum approximation whose absolute validity is limited for nanoscale powders. Because the optical and acoustic estimates are not thermodynamically equivalent Debye temperatures in nanocrystalline systems, their absolute magnitudes should

Table 4 Debye parameters

Samples	x(mol)	θ_D^I (K)	θ_D^E (K)
$CoFe_2O_4$		686±2	418±2
$Co_{0.6}Zn_{0.4}Fe_{2-x}Bi_xO_4$	0.000	687±2	420±2
	0.005	688±2	420±2
	0.010	690±2	421±2
	0.030	691±2	425±2

not be over-interpreted. The load-bearing result of this study is the consistent compositional trend of both parameters increasing with x within uncertainty.

Crucially, the parallel increase of both θ_D^I and θ_D^E with Bi content directly reflects the enhanced rigidity and bonding strength of the doped lattice. Stronger interatomic bonds elevate the vibrational frequencies (shifting the phonon spectrum upward) and also increase the acoustic wave speeds, both of which contribute to a higher Debye temperature.

In essence, the higher θ_D indicates that Bi doping reinforces the lattice, raising its characteristic phonon cutoff. This has implications for applications: higher Debye temperature often correlates with improved thermal stability, so Bi-doped ferrites may perform better under high-temperature or high-frequency conditions. Future experiments (e.g. heat-capacity or thermal transport measurements) could directly verify the increased Debye temperature and related thermal properties.

4 Conclusions

Our FTIR analysis and IR-derived elasticity metrics indicate that nominal Bi addition ($x \leq 0.03$) produces a reproducible blue-shift of the octahedral vibrational contribution and an increasing trend in effective elastic parameters. Bi addition shifts the octahedral vibrational contribution to higher wavenumber and increases IR- derived modulus trends. Accordingly, the Debye parameters calculated from IR wavenumbers and from acoustic velocities increase with Bi content. The increasing Debye-parameter trends suggest improved vibrational energy scales with Bi addition, which may be relevant to thermal stability. These results elucidate the fundamental impact of heavy-ion substitution on ferrite lattice dynamics. They underscore FTIR spectroscopy as a powerful, non-calorimetric tool for probing elastic and thermal properties. Overall, our work highlights both the academic significance of linking dopant chemistry to lattice stability and the technological potential of Bi-doped Co-Zn ferrites in advanced magnetic and electronic devices requiring enhanced mechanical and thermal robustness. Finally, we emphasize that FTIR cannot confirm Bi site occupancy, detect trace secondary phases, or verify actual stoichiometry.

5 Authors' contributions

All authors contributed to the study conception and design. Material preparation was performed by Italo Nuta and Thiago Eduardo Pereira Alves. Experimental tests were carried out by Italo Nuta, Thiago Eduardo Pereira Alves and A. Franco Jr. Data collection and analysis were performed by Thiago Eduardo Pereira Alves, Prasun Banerjee and A. Franco Jr. The first draft of the manuscript was written by Thiago Eduardo Pereira Alves, Prasun Banerjee and A. Franco Jr. All authors read and approved the final manuscript.

6 Funding Information

We acknowledge the support of the INCT of Spintronics and Advanced Magnetic Nanostructure (INCT-SpinNanoMag), CNPq 406836/2022-1, and FAPEG Nº: 202410267000178. One of us (A.F.Jr.) is CNPq fellow under Grant No. 307510/2022-0.

7 Data Availability

All relevant data are within the paper. All relevant data are within the manuscript and its Additional files. No additional data are available. The data are available from the corresponding author on reasonable request.

8 Declarations

8.1 Ethics Approval

Not applicable.

8.2 Consent to Participate

Not applicable.

8.3 Consent for Publication

The authors consent to publish this article.

8.4 Conflicts of Interest

The authors declare that they have no known competing financial interests or personal relationships that could have appeared to influence the work reported in this paper.

References

[1] MH Abdellatif and AA Azab. Elastic properties of cr-doped mn ferrite. *Bulletin of the National Research Centre*, 43(1):111, 2019.

[2] KB Modi, MC Chhantbar, and HH Joshi. Study of elastic behaviour of magnesium ferri aluminates. *Ceramics international*, 32(2):111–114, 2006.

[3] Sagar E Shirsath, SM Patange, RH Kadam, ML Mane, and KM Jadhav. Structure refinement, cation site location, spectral and elastic properties of zn2+ substituted nife2o4. *Journal of molecular structure*, 1024:77–83, 2012.

[4] RD Waldron. Infrared spectra of ferrites. *Physical review*, 99(6):1727, 1955.

[5] Shyam K Gore, Rajaram S Mane, Mu Naushad, Santosh S Jadhav, Manohar K Zate, ZA Alothman, and Biz KN Hui. Influence of bi 3+-doping on the magnetic and mössbauer properties of spinel cobalt ferrite. *Dalton transactions*, 44(14):6384–6390, 2015.

[6] MH Abdellatif, AA Azab, and M Salerno. Effect of rare earth doping on the vibrational spectra of spinel mn-cr ferrite. *Materials Research Bulletin*, 97:260–264, 2018.

[7] SS Bhatu, VK Lakhani, AR Tanna, NH Vasoya, JU Buch, PU Sharma, UN Trivedi, HH Joshi, and KB Modi. Effect of nickel substitution on structural, infrared and elastic properties of lithium ferrite. *Indian Journal of Pure and Applied Physics*, 45(7):596–608, 2007.

[8] F Fakhry, E Shaheen, H El-Dosoky, TM Meaz, M Mubark, and R El-Shater. Elastic and magnetic characteristics of nano-spinel ferrite co0. 5 mgxcu0. 5- xfe2o4. *Scientific Reports*, 14(1):29407, 2024.

[9] TEP Alves, HVS Pessoni, and A Franco Jr. The effect of y 3+ substitution on the structural, optical band-gap, and magnetic properties of cobalt ferrite nanoparticles. *Physical Chemistry Chemical Physics*, 19(25):16395–16405, 2017.

[10] Khalid Mujasam Batoo, Muhammad Hadi, Ankush Chauhan, Ritesh Verma, Mahavir Singh, Omar M Aldossary, and Gagan Kumar Bhargava. High-frequency applications of bismuth-doped co–zn ferrite nanoparticles for electromagnetic interference filter and multilayer inductor chip fabrication. *Applied Physics A*, 128(4):283, 2022.

[11] SA Mazen, SF Mansour, E Dhahri, HM Zaki, and TA Elmosalami. The infrared absorption and dielectric properties of li–ga ferrite. *Journal of alloys and compounds*, 470(1-2):294–300, 2009.

[12] KB Modi, JD Gajera, MP Pandya, G Vora, and HH Joshi. Far-infrared spectral studies of magnesium and aluminum co-substituted lithium ferrites. *Pramana*, 62(5):1173–1180, 2004.

[13] KB Modi. Elastic moduli determination through ir spectroscopy for zinc substituted copper ferri chromates. *Journal of Materials Science*, 39(8), 2004.

[14] SL Kakani and C Hemrajani. Text book of solid state physics. *Sultan Chand & Sons, New Delhi*, 1997.